materials

MDPI

Article

An Investigation of Non-Linear Strength Characteristics of Solidified Saline Soils in Cold Regions

Qian Ding [1], Zheng Hu [1], Shuai Huang [2], Kezheng Chen [3], Yanjie Liu [1,4,*] and Lin Ding [1,3,4]

[1] School of Hydraulic and Electric Power, Heilongjiang University, Harbin 150080, China
[2] School of Forestry, Northeast Forestry University, Harbin 150040, China
[3] College of Engineering and Technology, Northeast Forestry University, Harbin 150040, China
[4] School of Civil Engineering, Heilongjiang University, Harbin 150080, China
* Correspondence: 1996058@hlju.edu.cn

Abstract: To date, the modelling of constitutive equations of solidified frozen saline soil have seldom been studied. This paper presented the formulation of a damage constitutive model for solidified saline frozen soil considering both freeze thaw cycles (FTCs) and salinities. To model the solidified frozen saline soil, the unconfined compression strength test (UCST) and consolidated undrained (CU) triaxial shear test were conducted under three ambient temperatures (20, –10, and –20 °C), five ages (3, 7, 14, 28, and 90 d), six salinities (0, 1, 2, 3, 4, and 5%), and four FTCs (0, 5, 10, and 14 times) in this research. The UCST results showed that the unconfined compressive strength (UCS) of the solidified saline soils at an age of 14 days can reach 75% of the maximum UCS, which basically meets the engineering construction requirements. The range of the rate of strength loss as affected by salinity was 16.2% to 75.65%, while the coupling effect of salt and frozen conditions amplified the rate of strength loss. Affected by increasing salinity, the rate of strength loss of frozen soils was magnified by a factor of 1.2 to 3.7 compared to thawing soils. Likewise, the CU triaxial shear test showed that the rate of strength loss of shear strength was amplified by the coupling effect of FTCs and salt erosion. With increased FTCs, the strain threshold of Young's modulus was gradually pushed backward, which was similar to the effect of salinity. Remarkably, the damage constitutive model performed better than conventional constitutive models for the solidified saline soil under the salt–freezing coupling effect.

Keywords: solidified saline soil; cold regions; freeze–thaw cycles; damage models; Weibull distribution

check for updates

Citation: Ding, Q.; Hu, Z.; Huang, S.; Chen, K.; Liu, Y.; Ding, L. An Investigation of Non-Linear Strength Characteristics of Solidified Saline Soils in Cold Regions. *Materials* **2022**, *15*, 7594. https://doi.org/10.3390/ma15217594

Academic Editor: Changho Lee

Received: 29 September 2022
Accepted: 24 October 2022
Published: 28 October 2022

Publisher's Note: MDPI stays neutral with regard to jurisdictional claims in published maps and institutional affiliations.

Copyright: © 2022 by the authors. Licensee MDPI, Basel, Switzerland. This article is an open access article distributed under the terms and conditions of the Creative Commons Attribution (CC BY) license (https://creativecommons.org/licenses/by/4.0/).

1. Introduction

China has the third-largest frozen ground region in the world, and frozen ground covers about 56.3% of the land area in China [1,2]. Climate change has greatly affected the infrastructure in frozen ground locations, causing problems such as mud pumping-induced cracks and frost-related heaving on roads, and landslides induced by freeze–thaw [3–6]. Meanwhile, the second-largest frozen ground region and the largest carbonate-stained land area, of approximately 3.2×10^4 km^2, is located in Northeast China. Influenced by freeze–thaw cycles (FTCs) and salinization, the physical properties of the soil have suffered great deterioration [7,8]. With the economic development of society, engineering construction in cold regions is gradually receiving more and more attention from researchers, and the engineering of cold region saline soils represents a major challenge for the geotechnical engineering community. Therefore, research on the salt–thermal coupling of frozen soil is of great importance [9–11].

Recently, a large number of research studies have focused on the effects of FTCs on soil. Experimental testing showed that the macrophysical properties of soil were significantly influenced by FTCs. For example, the UCS and shear strength of soil deteriorated with the development of FTCs process [12]. The soil porosity and saturated hydraulic conductivity

gradually increased following subjection to 30 FTCs. The microphysical properties of soil, such as the pore size, microstructure, and texture, were similarly impacted by the FTCs effects [13]. These effects of FTCs can have a superimposed effect with salt erosion and show strong non-linear physical properties [14]. Therefore, study on the mechanism of this deterioration effect is extremely important in engineering construction.

The poor physical properties of saline soil increase the likelihood of engineering geological hazards; these include melt sinking, salt heaving, and salt corrosion [15]. Therefore, engineers usually take certain foundation treatment measures (e.g., landfill replacement, solidified saline soil, and compacted soil) to ensure that the infrastructure is safe for building on saline ground [16–18]. In the past, researchers have carried out a large number of studies on saline soil improvement. Generally speaking, saline soil improvement methods have typically included physical improvement, chemical improvement, electro-osmosis improvement, and biological improvement [19–29].

Among the chemical improvement methods, the most typical and economical is the inorganic improvement method, in which lime, fly ash, and cement are added to the soil to improve its physical properties through a series of hydration reactions and the reconstitution of the soil skeleton [30–32]. This method is widely used in the engineering construction process [33–35]. Previous works have shown that the inorganic improvement method is significantly effective in dealing with the effect of saline erosion and FTCs, and markedly enhances the mechanical properties of saline soil [36–39]. Research on the physical properties of the inorganic improvement of saline soil under FTCs has a substantial prospect of engineering application.

Although previous research has shown that inorganic amendments are very economical and effective means of improving the strength of saline soils [40,41], most of the research has focused on the variation patterns of macromechanical properties and the microstructural characteristics [42,43], and few researchers have carried out research on the modelling of solidified saline soils. Traditional strength criteria and constitutive models have rarely been applied to the study of saline soil under the effect of FTCs [44–50]. In addition, due to the complexity of the modified saline–alkali soil as an artificially remodeled soil structure, its compaction and strength are high, and the stress damage has elastic-brittle characteristics similar to concrete, as well as the stress characteristics of a soil body [51]. Meanwhile, caused by the effect of FTCs and the effect of water salt migration, the saline soil exhibited complex physical properties, leading to irreversible damage to soils [52,53]. Thus, it is difficult to use a model to describe the mechanical properties of improved saline soils under the effect of FTCs.

In the vast frozen saline ground, engineers are desperate to find reliable physical models of modified saline soil under the effect of FTCs and to solve the engineering problem of the coupling effect of frost and salt leading to complex strength deterioration. Considering that the physical properties of the modified saline–alkali soil are between concrete and soil, this paper takes improved saline–alkali soil as the research object and draws on the concrete damage principal theory, combined with the actual mechanical properties of improved soil, to study the damage evolution law under the coupling effects of freezing and salt load conditions.

2. Test Materials and Methods

2.1. Test Materials

Test soil was taken from the Songnen Plain (126.28 °E, 46.65 °N) at a depth of 2.0~4.0 m below the existing ground surface. Based on the Standard of Test Methods of Soil for Highway Engineering (JTC3430-2020), the specific gravity of the soil was measured by density bottle methods, the liquid–plastic limit of the soil was determined by the liquid–plastic limit combined device, and the uniformity coefficient and coefficient of curvature were calculated by the size distribution test. Its main physical properties are shown in Table 1. For this study, the test soil samples were prepared manually as carbonate saline soil. The inorganic amendments used in the tests were lime, ordinary silicate cement, and

primary fly ash. The lime is calcium lime powder with CaO content of 82.4%, produced by Yichun Huihui Technology Co., Ltd., Xinyu, China, the cement is P42.5 produced by YATAI Group Harbin Cement Co., Ltd., Harbin, China, and the primary fly ash selected was low calcium fly ash with a particle size of 42 μm and a burn vector of 2.02%, produced by Heilongjiang Thermal Power Company, Harbin, China. The main oxides are shown in Table 2.

Table 1. Average values of basic physical and mechanical properties of soils.

Specific Gravity (g/cm^3)	Optimum Moisture Content (%)	Dry Density (g/cm^3)	Liquid Limit (%)	Plastic Limit (%)	Plastic Limit Index	Uniformity Coefficient	Coefficient of Curvature
1.8	16.6	1.7	33	21	12	6.04	1.4

Table 2. Chemical composition of inorganic improvers.

Chemical Composition	SiO_2	CaO	MgO	SO_3	Loss on Burn	Al_2O_3	Fe_2O_3
Lime	3.5	82.4	7.3	0.6	2.0	/	/
Fly ash	51	3.87	0.93	0.60	1.44	32.30	7.56
Cement	21	59	≤1.5	≤0.3	≤0.5	15.1	4.2

2.2. Experimental Program

The tests were conducted using the WDW-100 uniaxial produced by Jinan ShiDaiShiJin Testing Machine Co., Ltd., Jinan, China, and GDS advanced dynamic and static permafrost triaxial test systems developed by the GDS, UK. The compressive strength test soil sample was based on a triple-ash solidified saline soil with a mass ratio of 3:4:6:87 of lime, cement, fly ash, and saline soil. The factors of temperature, age, and salinity were set to simulate a cold temperature environment. For this purpose, 180 specimens were made for UCST and 72 specimens were made for CU triaxial shear test. The diameter of the test sample was 39.1 mm and the height was 80 mm. To ensure the accuracy of our tests, the mass error of all specimens was controlled within 2 g and the height was controlled within 2 mm. The test factors and levels are shown in Table 3.

Table 3. Factors and levels.

	Factor	Levels
Stage 1	Temperature (°C)	20/−10/−20
	Age (d)	3/7/14/28/90
	Salinity (%)	0/1/2/3/4/5
	Freeze–thaw cycles (times)	0/5/10/14
Stage 2	Salinity (%)	1/2/3
	Confining pressure (MPa)	0.1/0.3/0.5/0.8/1.0/1.5

2.3. Experimental Methods

In road pavement sub-base construction, the unconfined compressive strength of solidified saline soils at different ages acts as an important basis for judging whether the strength requirements of the pavement sub-base are met. Therefore, this research used a microcomputer-controlled electronic universal testing machine (WDW-100E) to test the unconfined compression resistance of solidified saline soil, with the press descending at a rate of 2.0 mm/min. The microcomputer automatically collected the test data every 2 s, continuing after the peak pressure, with a 4% to 5% strain stop. The consolidated undrained test was carried out using the GDS advanced dynamic static frozen soil triaxial test system, prepared, maintained, and freeze–thaw cycled in accordance with the specifications, with the specimens being saturated by vacuum extraction followed by backpressure saturation to ensure a saturation of 90% or more before testing. The consolidation process was isotropic

consolidation with a shear rate of 0.08 mm/min. The test factors and levels are shown in Table 3.

3. Test Results and Analysis

3.1. UCST Results

Figure 1 shows the stress–strain curves and damage patterns of the specimens at an age of 14 d. The stress–strain curve can be divided into five stages. Stage 1, with salinity equal to 0, for example, is the compaction stage (OA), where the pores of the solidified saline soil start to close with increasing pressure and become smaller in volume. Stage 2 is the elastic deformation stage (AB), where the stress–strain relationship is linear. After the OA stage of compaction, the original pore space is further compressed, and no cracks are produced at this stage. After further compaction, the solidified saline soil starts to produce cracks, the longitudinal volume starts to become larger, and the slope of the curve starts to become smaller, which means that the stress growth rate is smaller than the strain growth rate. After point C the slope of the curve changes less rapidly and the resulting crack quickly becomes larger and more voluminous; this is the fourth stage, known as the damage stage (CD). The fifth stage, after point D, is referred to as the post-damage stage. As the salinity rises, the compaction stage becomes longer, the elastic stage becomes shorter, the yield limit value becomes lower, and the specimen crumbles significantly in the post-damage stage.

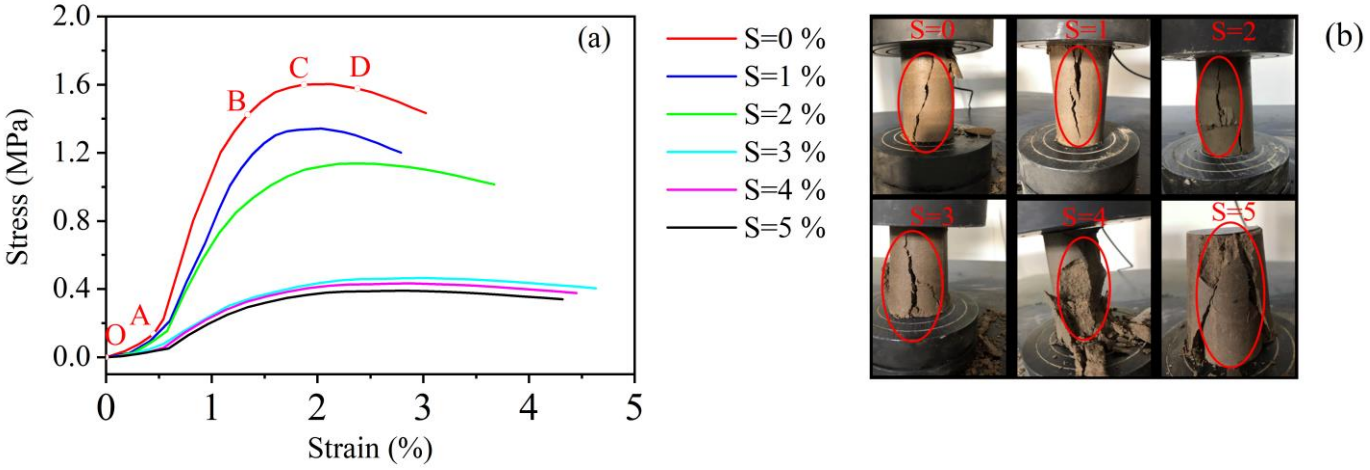


Figure 1. (**a**) Types of stress–strain curves (S represents salinity) and (**b**) compressive failure types for solidified saline soils with different salinities at an age of 14 days.

As shown in Figure 2, when the age is more than 7 d, the UCS of solidified saline soils decreases with increasing salinity, and the rate of strength loss *K* increases with increasing salinity. At an age of 3 d, with increasing salinity, the UCS exhibits a decreasing trend followed by an increasing trend. Thus, when the age is brief, the water in the soil does not fully participate in the hydration reaction, while the salinity is low and the salt is almost completely dissolved in the water; then, as the salinity increased, the salt produces a deteriorating effect in the soil; as the salinity exceeds the brine saturation threshold, and then as the salinity increases, the salt will precipitate in the water and become part of the soil skeleton structure, increasing the UCS. Meanwhile, when the age is lengthy, the hydration reaction occurs in its entirety, and the hydration reaction causes the soil pores to be completely filled, producing compact soil. At this time, with increasing salinity the degree of salt erosion to the soil skeleton structure gradually increases.

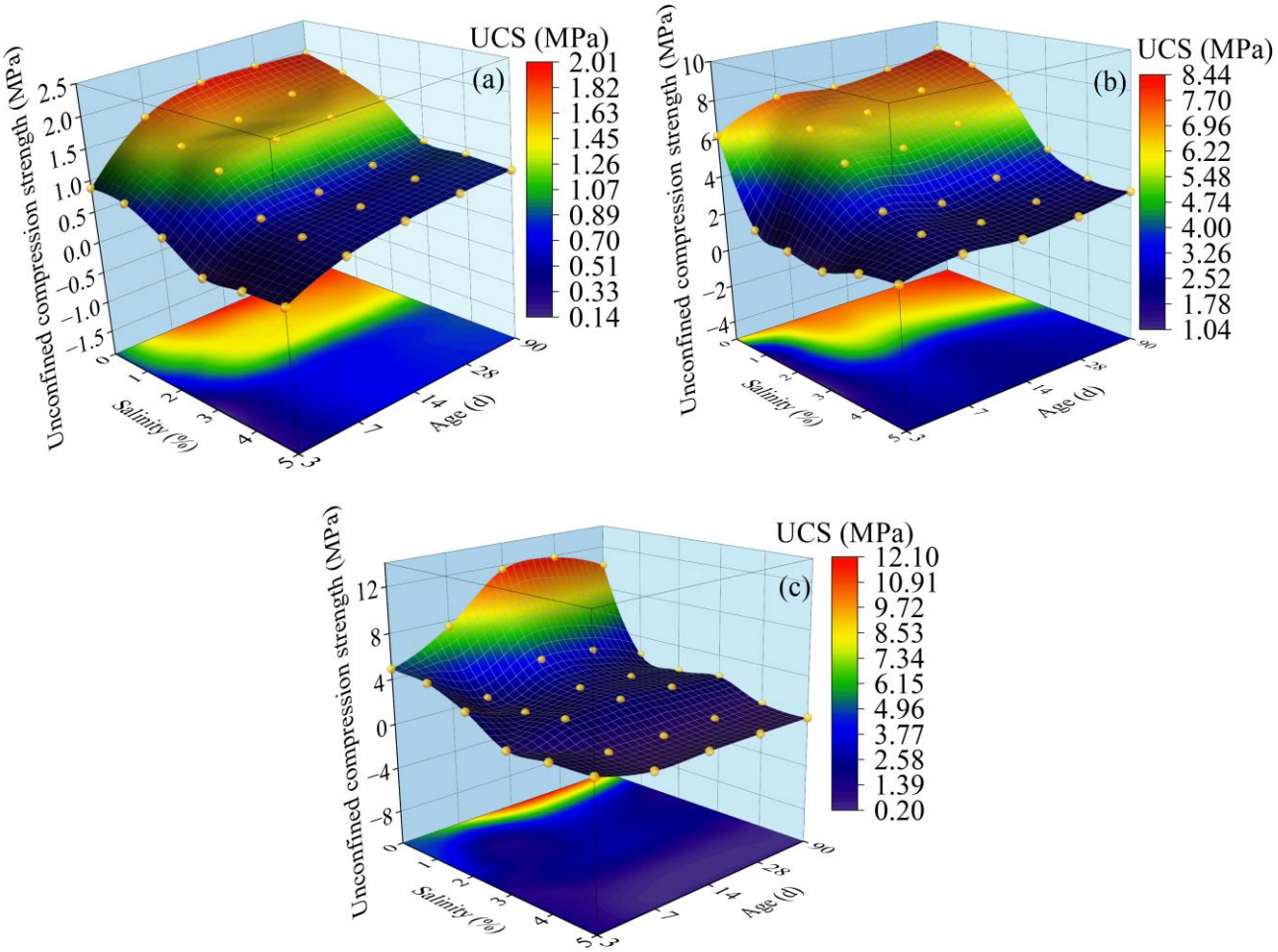


Figure 2. Effect of salt content and age on compressive strength of improved soils. Notes: (**a**) Ambient temperature of unconfined compression test (UCST) at 20 °C; (**b**) ambient temperature of UCST at −10 °C; (**c**) ambient temperature of UCST at −20 °C.

3.2. The Rate of Strength Loss

In order to analyze the effect of salinity on the UCS of solidified saline soils, the rate of strength loss due to salinity, *K*, is defined as follows:

$$K = \frac{q_{0max} - q_{imax}}{q_{0max}} \times 100\% \quad (1)$$

where *K* is a dimensionless constant, q_{0max} is the maximum UCS with a salinity of zero, and q_{imax} is the maximum UCS for different salinities.

In Figure 3, the results of the rate of strength loss show that the rate of strength loss increased with the decreasing of temperature and the increasing of salinity when the age was more than 7 days. It is clear that the salt–freezing coupling effect will amplify the rate of strength loss. On the one hand, the lower the temperature, the more significant the frost heave effect on the soil. One the other hand, the low temperature produces lower brine saturation. Under the effect of frost heave, the soil becomes very dense; however, affected by low temperature, the crystallization of salt breaks down the dense soil structure and reduces the strength of the soil [54].

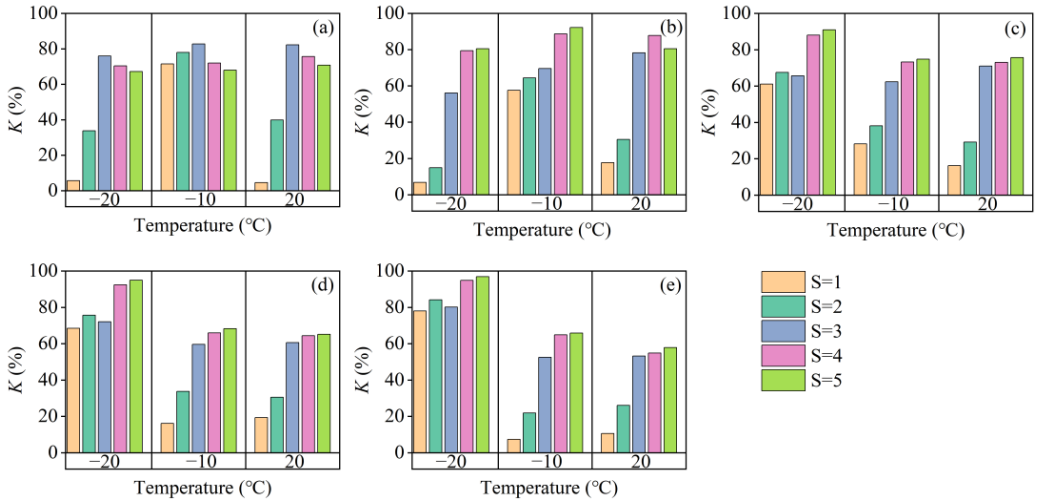


Figure 3. Rate of strength loss by salinity, with temperatures and ages. (**a**) Under the age of 3 days; (**b**) under the age of 7 days; (**c**) under the age of 14 days; (**d**) under the age of 28 days; (**e**) under the age of 90 days.

3.3. Age–Strength Relationships

As indicated in Figure 2, the UCS of solidified saline soils increases with age at temperatures above −20 °C and salinities below 4%. This is due to a series of hydration reactions occurring during the curing process of solidified saline soils. At this point, the soil skeleton of the lower salinity specimens consisted mainly of the hydration reaction products of the curing agent. For salinities greater than or equal to 4%, the compressive strength at an age of 3 d was greater than that at age 7 d. This is because the reaction rate of $NaHCO_3$ and $Ca(OH)_2$ is faster than the hydration reaction rate of the curing agent, which preferentially produces the soil skeleton [55]. However, as the age of the curing agent increases, the hydration reaction products are broken down before the soil skeleton can re-form, which causes the compressive strength curves of specimens with a salinity level of greater than 4% to first decrease and then increase. This means that when saline soils cured with inorganic amendments exceeding 4% are still cured at a strength of 3 d to 7 d according to conventional construction guidelines, this will cause significant damage to the project. In order to avoid this hazard, it is necessary to refer to the strength after 14 d of curing.

4. Non-Linear Strength Characterization

4.1. Changes in the Stress–Strain Relationship for Improved Soils for Different FTCs and Salinities

The slope of the stress–strain curve for improved soils under different FTCs and different salinities is shown in Figure 4. The slope of the stress–strain curve for improved soils under the same FTC and the same salinity gradually increases with an increase in the confining pressure. The slope of the stress–strain curve decreases significantly with an increase in salinity when FTCs = 0, because the soil is improved when the salinity equals 1% and the internal structure is tight; when the salinity increases, pores develop in the solidified soil and there are fillers in the pores [56]. The slope of the stress–strain curve decreases significantly with a confining pressure (CP) $\leq$ 0.5 MPa, and with a CP $\geq$ 0.8 MPa, the internal pores of the soil are closed and the slope of the stress–strain curve does not change significantly.

With the increasing of FTCs, the deformation resistance of the solidified soil decreases. Taking a CP equal to 1.5 MPa as an example, the shear strength at 5, 10, and 14 FTCs for a salinity equal to 1% decreases by approximately 47.3%, 52.6%, and 59.6%, respectively, compared to FTC of 0 times. The shear strengths at a salinity of 2% decrease by 3.6%, 15.5%, and 35.5%, respectively, for increasing FTCs, while those at a salinity of 3% decrease by 8.7%, 23.1%, and 34.6%, respectively, for increasing FTCs. This phenomenon is due to the

temperature gradient inside the soil during the FTC. The water moves with the salt to the lower end of the temperature gradient, and the movement of the water and salt damages the internal structure of the solidified soil.

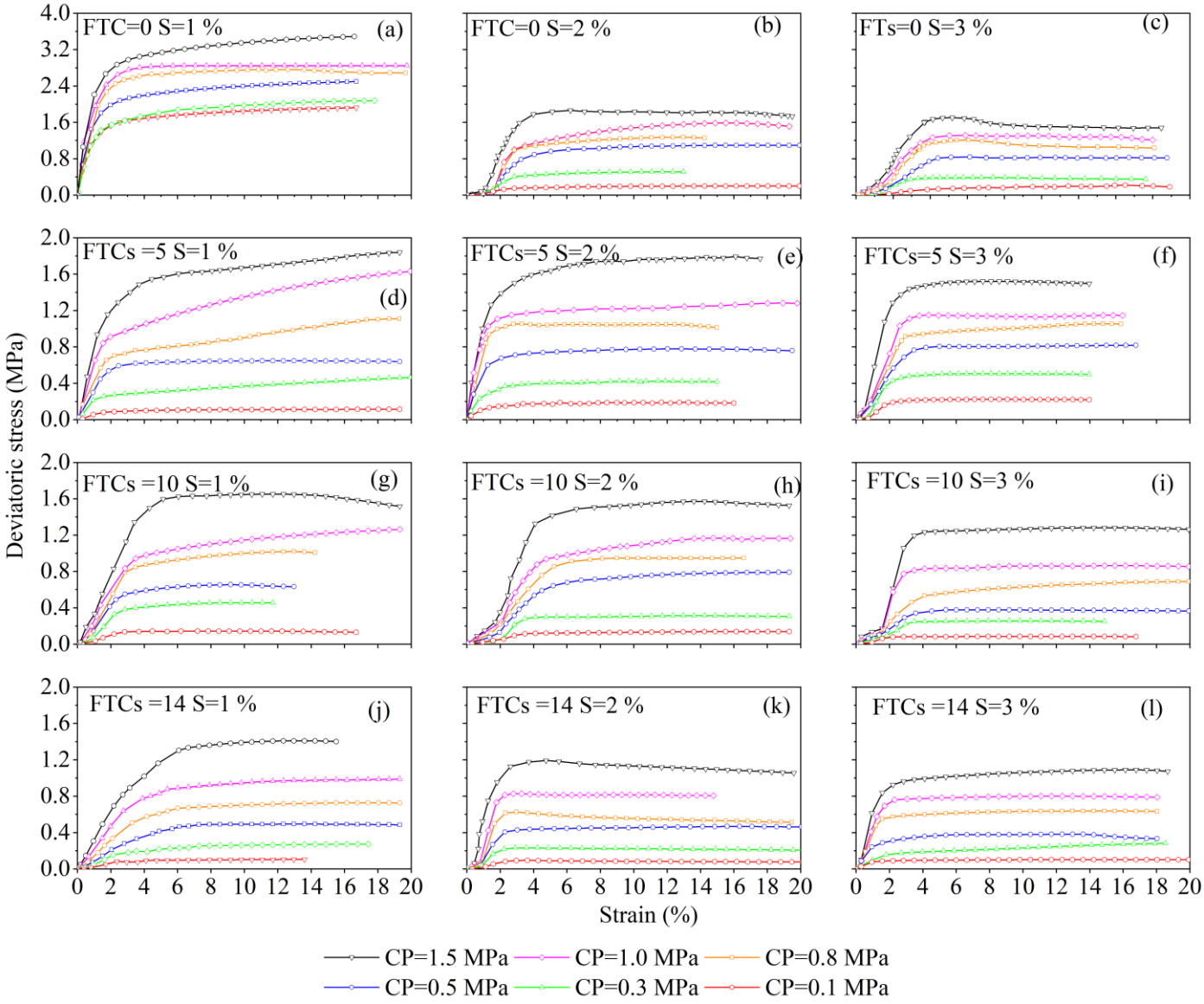


Figure 4. Bias stress–axial strain curves for different freeze–thaw cycles and different salinity content. Notes: FTCs represents freeze–thaw cycles, S represents salinity, and CP represents confining pressure.

Figure 4 shows that the stress–strain relationship of the saline soil with a salinity equal to 1% indicates either strain hardening or weak strain softening; with increasing salinity the stress–strain curve shows weak strain softening. After the FTCs, the stress–strain relationship of the improve solidified soils showed weak strain hardening and did not change rapidly to strain softening, as noted in the literature [57,58], which indicates that the improvement significantly increased the frost resistance of the saline soils.

4.2. Effect of FTCs and Salt Erosion on the Tangent Modulus of Solidified Soils

Figure 5 shows the tangent modulus E_s for different salinities at different confining pressures; E_s is an important parameter for measuring a soil's resistance to deformation. Based on the results of the stress–strain relationship test, the tangent modulus can be calculated for different confining pressures, where the maximum calculated tangent modulus is generally referred to as Young's modulus. The larger the confining pressure, the larger

the tangent modulus. At a salinity of 1%, with an increase in shear stress, the tangent modulus decreases and becomes closer to a certain value. As salinity increases, the tangent modulus shows an increase followed by a decrease, the value of Young's modulus decreases significantly, and the strain corresponding to the Young's modulus becomes larger.

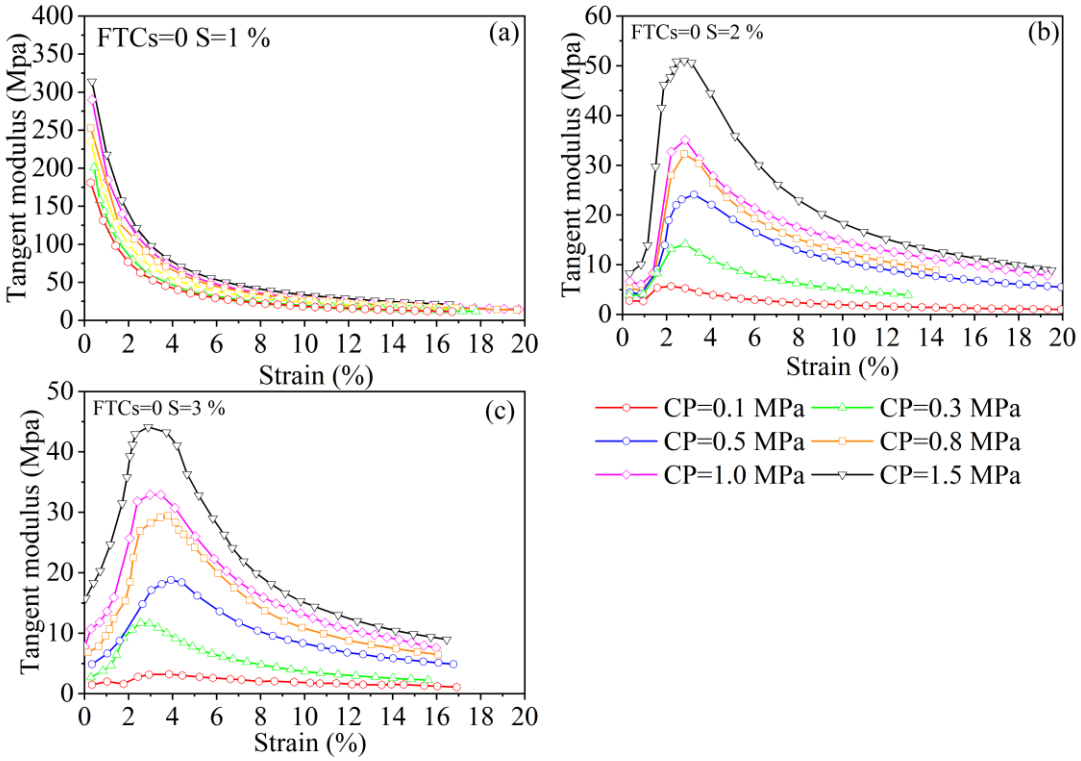


Figure 5. Tangent modulus E_s for different salinities at different confining pressures. Notes: FTCs represents freeze–thaw cycles, S represents salinity, and CP represents confining pressure.

Figure 6 shows the tangent modulus E_f for different FTCs with a salinity of 1% at different confining pressures. At five FTCs, the trend of the tangent modulus resembles that of the unfreeze–thaw; as the shear stress increases, the tangent modulus decreases, but Young's modulus decreases significantly, and the tangent modulus does not converge to a certain value. As the number of FTCs increases, Young's modulus continues to decrease and the decreasing trend begins to weaken. The trend of the tangent modulus resembles the trend of the tangent modulus for a salinity greater than 1%, which increases and then decreases. This suggests that FTCs and salinity damage solidified soils in a similar way, with both resulting in a reduction in strength due to additional loosening within the solidified soil.

Figure 7a shows the curves expressing the relationship between Young's modulus and salinity. The Young's modulus of the solidified soil shows different rates of decrease with increasing salinity under different confining pressures. Therefore, the Young's modulus–salinity curve for FTCs = 0 was chosen for analysis, and it was found that the following equation could be used to describe the relationship between E_s and salinity:

$$E_S = a \times x^b \quad (2)$$

where E_s is the Young's modulus, a and b are calculated parameters, and x is the salinity.

The data obtained from the tests were fitted with the Levenberg–Marquardt optimization algorithm to obtain the values of the calculated parameters a and b for the variation of the Young's modulus of solidified soil with salinity at different confining pressures, as shown in Table 4. The corresponding correlation coefficients were all greater than 0.977.

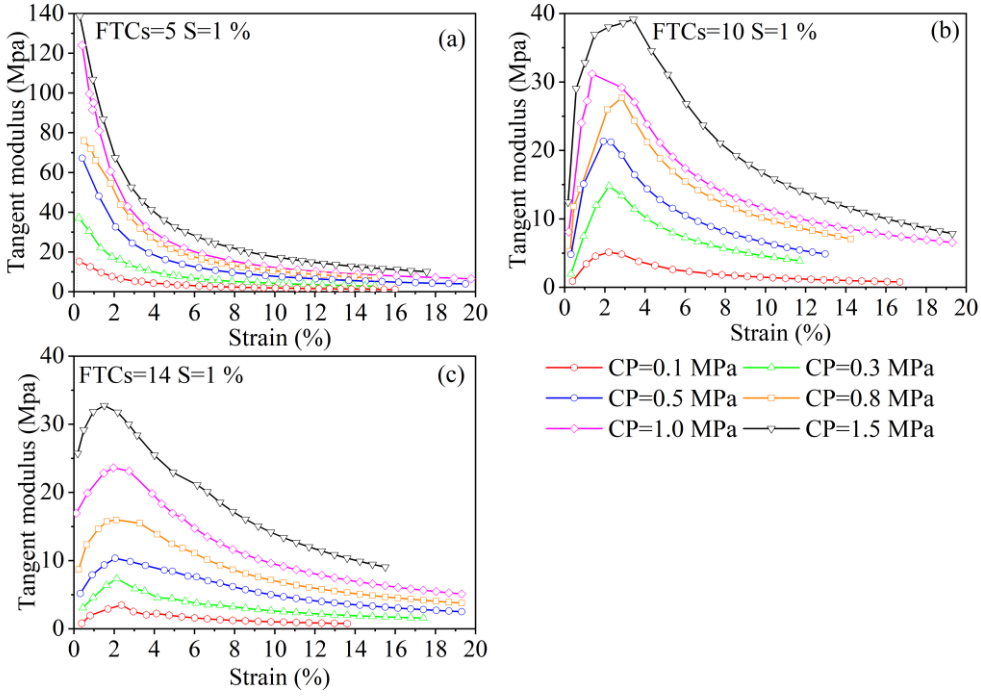


Figure 6. Tangent modulus E_f for different freeze–thaw cycles with a salinity of 1% at different confining pressures. Notes: FTCs represents freeze–thaw cycles, S represents salinity, and CP represents confining pressure.

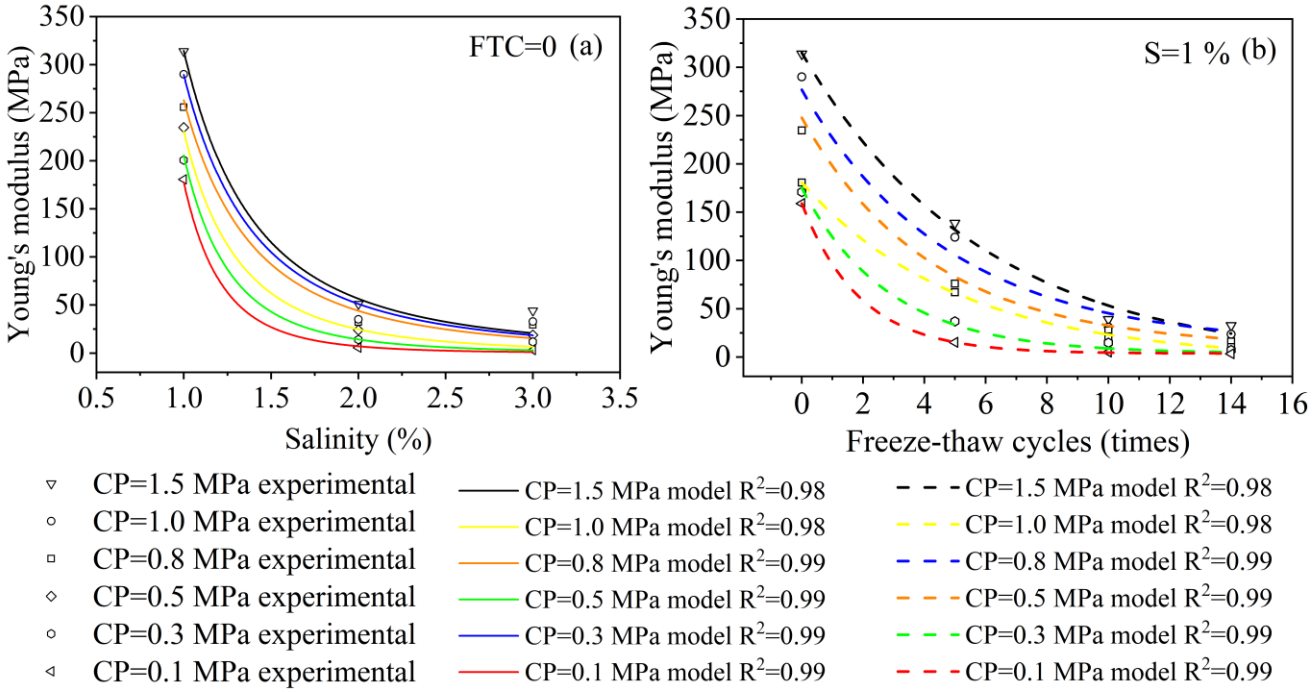


Figure 7. Comparison of test results and calculated results. Notes: FTCs represents freeze–thaw cycles, S represents salinity and CP represents confining pressure.

To simplify the analysis, using the data in Table 4, the relationship between the parameters a and b and the value of CP was obtained using multiple regression analysis as:

$$\mathrm{a} = -346.5x^2 + 1531.05x + 1629.17, \ (R^2 = 0.97) \quad (3)$$

$$\mathrm{b} = -2x^2 + 4.75x - 5.1,\ (R^2 = 0.95) \quad (4)$$

where x is the value of the confining pressure.

Table 4. Calculation of parameter a and b values.

CP/Mpa	a	b	R^2
0.1	1806.7	−4.9	1.00
0.3	2007.3	−3.6	0.99
0.5	2344.1	−3.0	0.99
0.8	2552.2	−2.6	0.98
1.0	2895.5	−2.5	0.98
1.5	3130.4	−2.3	0.94

Although the R^2 of the fitting curving are greater than 0.98, it may still be inaccurate due to the three points in salinities. Compared to similar studies [59], the fitting curving demonstrates increasing accuracy with an increase in salinity points. Figure 7a also shows a relative higher inaccuracy with high CP, which may due to the higher CP causing the pore space to reclose. As a result, the Young's modulus measured at 3% salinity is slightly greater than the predicted value at a high CP. This suggests that the prediction equations provided in this paper should be used to determine the relationship between Young's modulus and salinity for the solidified salt soils, taking into account whether the CP is too high.

Figure 7b shows the relationship between Young's modulus and the FTCs; under different CP, Young's modulus shows different decreasing rates with the increase of FTCs. The error of fitting curving showed a similar regulation in Figure 7a; the reason for this phenomenon is consistent with that previously mentioned. The following equation can be used to describe the relationship between Young's modulus and FTCs:

$$E_\mathrm{f} = a + b \times e^{\frac{-x}{c}} \quad (5)$$

where E_f is the Young's modulus; a, b, and c are calculated parameters; e is a constant; and x is the number of FTCs.

The data obtained from the tests were fitted with the Levenberg–Marquardt optimization algorithm to obtain the values of the calculated parameters a, b, and c for the variation of Young's modulus of solidified soil with the number of FTCs at different CP, as shown in Table 5. The corresponding correlation coefficients were all greater than 0.977.

Table 5. Calculated values for parameters a, b, and c.

CP (MPa)	a	b	c	R^2
0.1	26.5	1552.1	1.9	1.00
0.3	44.2	1635.4	3.0	0.99
0.5	54.7	1834.9	3.7	0.98
0.8	90.6	2268.4	4.2	1.00
1.0	117.7	2964.4	5.2	0.98
1.5	202.2	3203.9	5.9	0.98

Table 5 shows that the parameters a, b, and c all show a linear relationship with CP. To simplify the analysis, the following formula can be used to describe the relationship between parameters a, b, and c and CP:

$$\mathrm{D} = k\mathrm{CP} + \mathrm{H} \quad (6)$$

where D represents a, b, c, and k; H indicates the calculated parameter values; and CP represents confining pressure. The specific parameter values are shown in Table 6.

Table 6. Calculated parameter values *k*, H.

Parameter	*k*	H	R^2
a	124.3	2.3	0.96
b	1328.3	1313.3	0.93
c	2.8	2.0	0.94

4.3. Damage Evolution Equations and Intrinsic Structure Modelling

The damage variable under load is defined as D_n, and the damage variable under FTCs is D_f, which means that after N FTCs, the damage to the solidified soil caused by FTCs is characterized by the reduction of the initial elastic modulus:

$$D_f = 1 - \frac{E_f}{E_0} \tag{7}$$

New damage occurs when the stress level of the soil microelement exceeds a certain strength under load. The damage variable D_n under load is expressed as the ratio of failure microelement S_f to total microelement S after N FTCs:

$$D_n = \frac{S_f}{S} \tag{8}$$

When the total number of microelements S is large enough, Weibull distribution can be used to represent D_n. Therefore, we can allow the probability density function $\Phi(F)$ of the microelements after experiencing the FTC action to be as follows:

$$\Phi(F; m, F_0) = \frac{m}{F_0}\left(\frac{F}{F_0}\right)^{m-1} exp\left[-\left(\frac{F}{F_0}\right)^m\right] \tag{9}$$

where F is a randomly distributed variable indicating the microelement strength, and the Weibull distribution parameters m and T_0 reflect the changes in the average strength and elastic modulus for different FTCs.

Microelement strength is represented by F_n for a certain range of strengths, i.e., $[F_n, F_n + dF_n]$, the fracture between the microelements forms damage, and the number of damaged microelements in this process is S.

So, Equation (8) can be expressed as:

$$D_n = \frac{\int_{-\infty}^{F_n} S\Phi(x)dx}{S} = \int_{-\infty}^{F_n} \Phi(x)dx \tag{10}$$

Bringing Equation (9) into Equation (10), we obtain:

$$D_n = 1 - \exp\left[-\left(\frac{F_n}{F_0}\right)^m\right] \tag{11}$$

According to Lemaitre's stress–strain equivalence hypothesis [60], this is the same as the state of stress under damaged and under virtual non-destructive and effective strain for damaged elastic-brittle materials in the action of real strain ε, namely:

$$\varepsilon = \frac{\delta}{E^*} = \frac{\delta^*}{E} \tag{12}$$

In which:

$$\delta_c A_c = \delta_{cd} A_{cd} \tag{13}$$

$$\delta^* = \frac{\delta}{1 - D} \tag{14}$$

where E is the characteristic modulus of nondestructive materials, E^* is the characteristic modulus of destructive materials, δ is the effective stress acting on the damaged material, δ^* is the effective stress acting on the undamaged material, and D is the destructive variable. According to the strain equivalence principle extended by Zhang [61], for the undamaged state and the FTC state:

$$\delta_0 A_0 = \delta_f A_f \tag{15}$$

$$D_f = \frac{A_0 - A_f}{A_f} \tag{16}$$

where A_0 is the initial state of the microelement material-bearing effective area, A_f is the FTC state of the microelement material-bearing effective area, δ_0 is the effective stress of the initial undamaged microelement material, and δ_f is the FTC N times after the microelement material-bearing effective stress.

Equations (12)–(16) can be combined to obtain:

$$E_f = E_0(1 - D_f) \tag{17}$$

$$\delta_f = E_0(1 - D_f)\varepsilon_f \tag{18}$$

Equation (18) is the statistical damage model for FTCs if the soil pore space is completely closed due to the confining pressure, which suggests that the soil has reached the nondestructive state, i.e., $D_f = 0$.

At this time, the specimen after the FTC is taken as the reference state (undamaged state), and the strain equivalent principle is used again for the specimen under FTC load:

$$\delta_f A_f = \delta_n A_n \tag{19}$$

where A_n is the effective area of the microelement-bearing material in the load state after N FTCs and δ_n is the effective stress of the microelement-bearing material in the load state after N FTCs. Therefore, we obtain:

$$\delta_{fd} = E_f(1 - D_n)\varepsilon_n \tag{20}$$

where ε_n is the microelement material strain in the load state after N FTCs, and Equation (20) is the statistical damage model under FTC loading.

With the coupling of Equations (17) and (20), we obtain:

$$\delta_n = E_0(1 - D_{al})\varepsilon_n \tag{21}$$

where $D_{al} = D_n + D_f + D_f D_n$ indicates the total damage variable of the specimen under load after freeze–thaw cycling.

Substituting Equations (7), (11), and (20) into (21) and considering the influence of the initial damage threshold in the action of the FTCs and loads, the total damage evolution equation becomes:

$$D_{al} = \begin{cases} 1 - \frac{E_f}{E_0}, q < q_0 \\ 1 - \frac{E_f}{E_0} \exp\left[-\left(\frac{F_n}{F_0}\right)^m\right], q \geq q_0 \end{cases} \tag{22}$$

where q_0 is the initial damage stress threshold after N FTCs and q is the partial stress $q = \delta_1 - \delta_3$, where δ_1 is the maximum principal stress and δ_3 is the minimum principal stress.

From Equation (22), when the soil pores are completely closed due to the confining pressure, $E_f = E_0$, and the total damage evolution equation becomes only the damage equation under load.

In the initial stage of loading, the modified soil partial stress has not yet reached its damage threshold q_0, at which time the deformation of the modified soil microelement obeys Hook's law, i.e.:

$$\delta_1 = E\varepsilon_1 + v(\delta_2 + \delta_3) \tag{23}$$

where v is Poisson's ratio and E is the initial modulus of elasticity of the soil.

Since $\delta_2 = \delta_3$ in the conventional triaxial compression test, Equation (23) can be abbreviated as:

$$\delta_1 = E\varepsilon_1 + 2v\delta_3 \tag{24}$$

By combining Equations (14), (22), and (24), considering the influence of the initial damage threshold, the statistical damage equation under freeze–thaw cycle load is:

$$\delta_1 = \begin{cases} E_c\varepsilon_1 + 2v\delta_3, q<q_0 \\ E_c\varepsilon_1 \exp\left[-\left(\frac{F_n}{F_0}\right)^m\right] + 2v\delta_3, q \geq q_0 \end{cases} \tag{25}$$

As can be seen from Equation (25), to determine the damage variable D_{al}, it is necessary to solve the microelement strength F_n at the level of load after characterizing the FTC. Therefore, it is assumed that the micro-failure under the stress level after the FTCs should meet the effective stress and soil material parameters:

$$Fn - f\delta * e = 0 \tag{26}$$

where $\delta_e{}^*$ is the effective soil micro-cell stress and $f(\delta_e{}^*)$ is the micro-cell stress function. When $f(\delta_e{}^*) \geq F_n$, the stress level micro-unit body is damaged after the FTCs. According to the Mohr–Coulomb criterion:

$$\delta_1 - \delta_3\frac{1+\sin\varphi}{1-\sin\varphi} - \frac{2c\cos\varphi}{1-\sin\varphi} = 0 \tag{27}$$

where c and φ are the cohesion and the angle of internal friction, respectively. If the microelement strength F_n damage obeys the Mohr–Coulomb criterion, we have:

$$F_n = \delta_1^*(1-\sin\varphi) - \delta_3^*(1+\sin\varphi) \tag{28}$$

By combining Equations (28) and (24), an expression for the microelement strength of the soil with respect to the initial confining pressure can be obtained as:

$$F_n = (E\varepsilon_1 + 2v\delta_3)(1-\sin\varphi) - \delta_3^*(1+\sin\varphi) \tag{29}$$

The damage statistical model developed in this paper uses three-parameter Weibull distribution to describe the damage evolution equation for solidified soils, where the microelement strength F_n is determined by the strength criterion for geotechnical soils, i.e., Equation (29). Therefore, only the parameters m and F_0 need to be determined; these can be calculated from the characteristic points of the modified soil stress–strain curve. At different confining pressures, the solidified soil reaches its peak strength with a stress increment of 0, i.e., with:

$$\left.\frac{\partial\delta_1}{\partial\varepsilon_1}\right|_{\substack{\delta_1=\delta_m \\ \varepsilon_1=\varepsilon_m}} = 0 \tag{30}$$

where δ_m is the stress corresponding to the peak stress–strain curve of solidified soil and ε_m is the strain corresponding to the peak stress–strain curve of the solidified soil.

Differentiating Equation (25) and writing it according to Equation (22) can be simplified to:

$$m\left[-\left(\frac{F_n}{F_0}\right)^{m-1}\right] = \frac{F_0}{(1-\sin\varphi)} \tag{31}$$

When the solidified soil reaches its peak strength, its stress point should satisfy the following expression:

$$\delta_m = E_0(1-D_{al})\varepsilon_m \tag{32}$$

Combining Equations (31) and (32), we obtain:

$$\mathrm{m} = \frac{(E_0\varepsilon_\mathrm{m} + 2v\delta_3)(1-\sin\varphi) - \delta_3(1+\sin\varphi)}{(1-\sin\varphi)\mathrm{In}\left(\frac{\delta_\mathrm{m}}{\varepsilon_\mathrm{m}E_\mathrm{f}}\right)} \tag{33}$$

$$F_0 = \frac{(E_0\varepsilon_\mathrm{m} + 2v\delta_3)(1-\sin\varphi) - \delta_3(1+\sin\varphi)}{\mathrm{In}\left(\frac{\varepsilon_\mathrm{m}E_\mathrm{f}}{\delta_\mathrm{m}}\right)^{1/\mathrm{m}}} \tag{34}$$

It can be seen from Equation (33) that parameter m is positively correlated with F_0, and the influence of FTCs on the parameters is similar. Therefore, F_0 is taken as an example to show the influence of FTCs and CP on the parameters. As shown in Figure 8, the value of parameter F_0 without FTCs varies from 1.1 to 1.22. The greater the confining pressure, the greater the F_0. With an increase in FTCs, the growth rate of F_0 is related to the confining pressure. After five FTCs, the F_0 of CP = 1.5 increases by 48.4%, and the F_0 of CP = 0.1 only increases by 11.3%. After 14 cycles, the F_0 of CP = 1.5 increases by 147.6%, and the F_0 of CP = 0.1 increases by 94.2%.

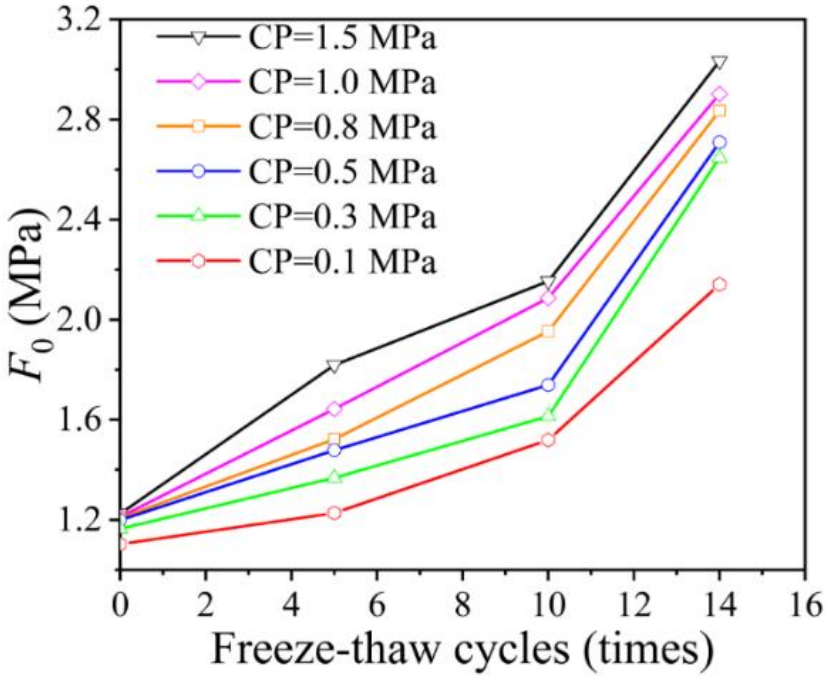


Figure 8. Effect of freeze–thaw cycles and confining pressure on F_0. Notes: CP represents confining pressure.

Now, bringing the model parameters into Equation (25), the solidified soil theoretical stress–strain curve considering the damage threshold value under FTC and load can be obtained and compared with the experimental curve, as shown in Figure 9. As seen in the figure, when the number of FTCs equals five, the total stress–strain curve is significantly lower than that of the samples with more than five FTCs, and the shear stress begins to decrease at this time. With increasing CP, the slope of the linear phase change curve increases significantly, and the threshold value of initial damage stress increases gradually. The lower the CP, the higher the visibility, which shows that high CP has the effect of reducing the initial damage caused by FTCs.

The experimental results are in good agreement with the theoretical calculation results. The theoretical results reflect the overall trend of the strength and deformation of the solidified saline soil under FTCs and loads with the number of FTCs and CP, indicating that the proposed freezing–thawing damage model of solidified soil can relatively reflect the entire stress–strain process in a temperature-alternating environment, and under external

load, even though it could be inaccurate under a high confining pressure inducing the effect of pore closure.

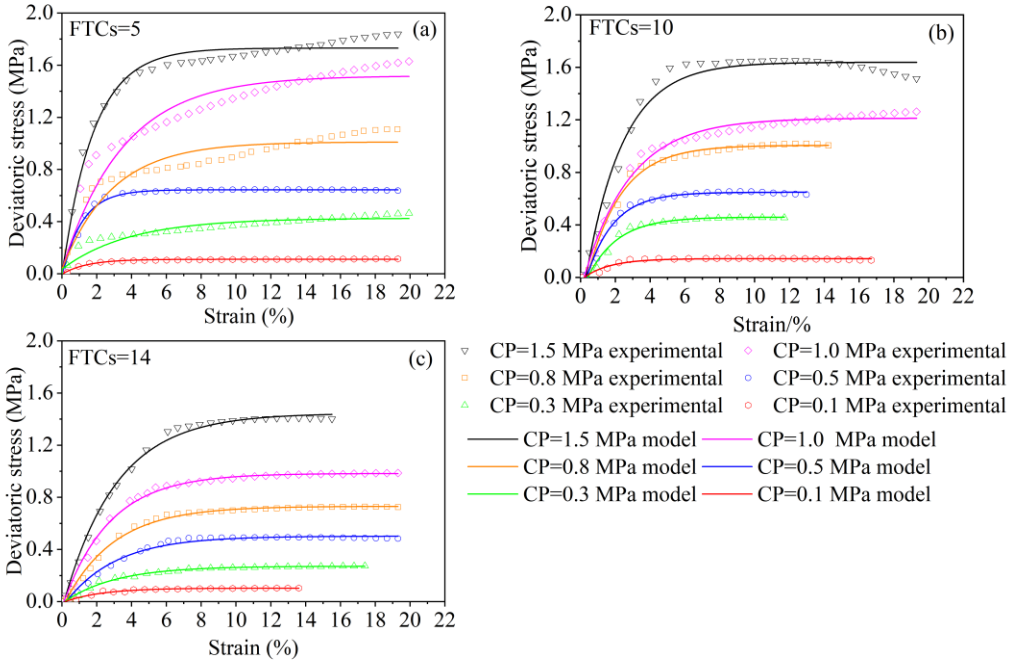


Figure 9. Theoretical stress–strain curves for calculated and tested values of solidified soils.

5. Conclusions

In this paper, the UCST of solidified saline soil was conducted in the laboratory at various salinities, temperatures, and ages, in order to analyze the coupling effect of freezing and salt. Young's modulus was investigated by CU triaxial tests, and a damage constitutive model based on Weibull distribution is proposed for solidified saline soil under the effect of FTCs. The main conclusions are as follows:

1. After using lime, fly ash, and cement to cure saline soils in cold regions, the UCS is greatly improved, and the solidified saline soils with a salinity of less than 3% can meet the requirements of the sub-base filler for secondary and lower roads with medium and light traffic at the age of 14 d. Both frost heave and salt erosion could cause irreversible damage in soil, and the coupling effect of freezing-salt will amplify the rate of strength loss.
2. After curing the saline soils in cold regions, the freeze–thaw resistance of the solidified saline soils is remarkably enhanced, and the stress–strain curve of the solidified saline soils does not show rapid strain softening after FTCs. The effect of FTCs and salt erosion causes peak stress to shift backward at the appearance of Young's modulus, which indicates that, with increased FTCs and salinity, the resistance to deformation of the solidified saline soil was reduced.
3. Considering the damage threshold of FTCs on solidified saline soil, Weibull distribution is used to describe its damage evolution regulation. The simulation results of modelling show that the damage constitutive model is more suitable than the traditional constitutive model for solidified saline soil under the effect of FTCs.

Author Contributions: Q.D. conceived the study. Q.D. and Y.L. analyzed the results and wrote the manuscript. Z.H., S.H., K.C. and L.D. assisted with data processing. All authors have read and agreed to the published version of the manuscript.

Funding: This work was supported by the National Natural Science Foundation of China (Grant No. 41071049). This work was also supported by the Open Fund of State Key Laboratory of Frozen Soil Engineering (Grant Nos. SKLFSE201919 and SKLFSE201802). This support is much appreciated.

Institutional Review Board Statement: Not applicable.

Informed Consent Statement: Not applicable.

Data Availability Statement: The data used to support the findings of this study are included within the article.

Acknowledgments: The authors are very grateful to Yanjie Liu and Lin Ding for their guidance. The authors are very appreciative of their efforts. Special thanks are also given to the two unidentified reviewers who have spent their precious time and efforts improving the quality of this paper.

Conflicts of Interest: The authors declare no conflict of interest.

References

1. Zhou, Y.W.; Guo, D.X.; Qiu, G.Q.; Zhang, T.J. *Geocryology in China*; Science Press: Beijing, China, 2000.
2. Ran, Y.H.; Li, X.; Cheng, G.D.; Zhang, T.J.; Wu, Q.B.; Jin, H.J.; Jin, R. Distribution of Permafrost in China: An Overview of Existing Permafrost Maps. *Permafr. Periglac. Process.* **2012**, *23*, 322–333. [CrossRef]
3. Wang, L.; Wang, H.; Tian, Z.; Lu, Y.; Gao, W.; Ren, T. Structural Changes of Compacted Soil Layers in Northeast China due to Freezing-Thawing Processes. *Sustainability* **2020**, *12*, 1587. [CrossRef]
4. Ma, Q.; Zhang, K.; Jabro, J.D. Freeze–thaw cycles effects on soil physical properties under different degraded conditions in Northeast China. *Environ. Earth Sci.* **2019**, *78*, 321. [CrossRef]
5. Wang, L.; Zuo, X.F.; Zheng, F.L.; Wilson, G.V.; Zhang, X.C.; Wang, Y.F.; Han, F. The effects of freeze-thaw cycles at different initial soil water contents on soil erodibility in Chinese Mollisol region. *Catena* **2020**, *193*, 104615. [CrossRef]
6. Wang, S.; Ding, J.; Xu, J.; Ren, J.; Yang, Y. Shear Strength Behavior of Coarse-Grained Saline Soils after Freeze-Thaw. *KSCE J. Civ. Eng.* **2019**, *23*, 2437–2452. [CrossRef]
7. Bureau JPLA. *Land Resources in Jilin Province*; Geological Publishing House: Beijing, China, 1994.
8. Wang, Z.Q. *Saline Soil in China*; Science Press: Beijing, China, 1993.
9. Li, G.Y.; Wang, F.; Ma, W.; Fortier, R.; Mu, Y.H.; Zhou, Z.W. Field observations of cooling performance of thermosyphons on permafrost under the China-Russia Crude Oil Pipeline. *Appl. Therm. Eng.* **2018**, *141*, 688–696. [CrossRef]
10. Wang, F.; Li, G.Y.; Ma, W.; Mu, Y.H.; Zhou, Z.W.; Mao, Y.C. Permafrost thawing along the China-Russia Crude Oil Pipeline and countermeasures: A case study in Jagdaqi, Northeast China. *Cold Reg. Sci. Technol.* **2018**, *155*, 308–313. [CrossRef]
11. Yang, S.Z.; Wen, X.; Zhao, L.; Shi, Y.L.; Jin, H.J. Crude Oil Treatment Leads to Shift of Bacterial Communities in Soils from the Deep Active Layer and Upper Permafrost along the China-Russia Crude Oil Pipeline Route. *PLoS ONE* **2014**, *9*, e96552. [CrossRef]
12. Lyu, C.; Nishimura, S.; Amiri, S.A.G. Pore-water pressure development in a frozen saline clay under isotropic loading and undrained shearing. *Acta Geotech.* **2021**, *16*, 3831–3847. [CrossRef]
13. Ma, Q.G.; Lai, Y.M.; Zhang, M.Y. Freezing-thawing behavior of saline soil with various anti-saline measures. *Eur. J. Environ. Civ. Eng.* **2019**, *23*, 1178–1202.
14. Wang, J.; Wang, Q.; Kong, Y. Analysis of the pore structure characteristics of freeze-thawed saline soil with different salinities based on mercury intrusion porosimetry. *Environ. Earth Sci.* **2020**, *79*, 161. [CrossRef]
15. Peng, W.; Wang, Q.; Zhang, X.D. Prediction of the structural yield strength of saline soil in western jilin province, China: A comparison of the back-propagation neural network and support vector machine models. *Symmetry* **2020**, *12*, 1163. [CrossRef]
16. Li, G.Y.; Yu, W.B.; Ma, W.; Qi, J.L.; Jin, H.J.; Sheng, Y. Experimental study of characteristics of frost and salt heaves of saline highway foundation soils in seasonally frozen regions in Gansu Province. *Rock Soil Mech.* **2009**, *38*, 2276–2280.
17. Wardeh, G.; Mohamed, M.A.; Ghorbel, E. Analysis of concrete internal deterioration due to frost action. *J. Build. Phys.* **2011**, *35*, 54–82. [CrossRef]
18. Zhang, Y.; Fan, J.H.; Liu, J.K.; Xu, A.H. Field tests on reinforcement effects of ground treatment of composite foundation in saline soils by dynamic compaction replacement. *Chin. J. Geotech. Eng.* **2011**, *33*, 251–254.
19. Virkutyte, J.; Sillanpää, M.; Latostenmaa, P. Electrokinetic soil remediation—Critical overview. *Sci. Total Environ.* **2002**, *289*, 97–121. [CrossRef]
20. Estabragh, A.R.; Naseh, M.; Javadi, A.A. Improvement of clay soil by electro-osmosis technique. *Appl. Clay Sci.* **2014**, *95*, 32–36. [CrossRef]
21. Flora, A.; Gargano, S.; Lirer, S.; Mele, L. Effect of electro-kinetic consolidation on fine grained dredged sediments. *Procedia Eng.* **2016**, *158*, 3–8. [CrossRef]
22. Eskisar, T.; Altun, S.; Kalipcilar, I. Assessment of strength development and freeze-thaw performance of cement treated clays at different water contents. *Cold Reg. Sci. Technol.* **2015**, *111*, 50–59. [CrossRef]
23. Lv, Q.F.; Jiang, L.S.; Ma, B.; Zhao, B.H. A study on the effect of the salinities on the solidification of sulfate saline soil solidified with an alkali-activated geopolymer. *Constr. Build. Mater.* **2018**, *176*, 68–74. [CrossRef]
24. Li, M.; Chai, S.X.; Du, H.P.; Wang, C. Effect of chlorine salt on the physical and mechanical properties of inshore saline soil treated with lime. *Soils Found.* **2016**, *56*, 327–335. [CrossRef]
25. Yu, H.Y.; Zhao, J.; Yang, J.J.; Li, Y.Q. Research on the mechanical properties and mechanism of alkali-activated saline soil composite materials. *Ferroelectrics* **2018**, *529*, 49–58.

26. Janoo, V.C.; Firicano, A.J.; Barna, L.A. Field testing of stabilized soil. *J. Cold Reg. Eng.* **1999**, *13*, 37–53. [CrossRef]
27. Arasan, S.; Nasirpur, O. The effects of polymers and fly ash on unconfined compressive strength and freeze-thaw behavior of loose saturated sand. *Geomech. Eng.* **2015**, *8*, 361–375. [CrossRef]
28. Gullu, H.; Hazirbaba, K. Unconfined compressive strength and post-freeze-thaw behavior of fine-grained soils treated with geofiber and synthetic fluid. *Cold Reg. Sci. Technol.* **2010**, *62*, 142–150. [CrossRef]
29. Yang, Z.J.; Still, B.; Ge, X. Mechanical properties of seasonally frozen and permafrost soils at high strain rate. *Cold Reg. Sci. Technol.* **2015**, *113*, 12–19. [CrossRef]
30. Ying, Z.; Cui, Y.-J.; Benahmed, N.; Duc, M. Changes in microstructure and water retention property of a lime-treated saline soil during curing. *Acta Geotech.* **2022**, *17*, 319–326. [CrossRef]
31. Tang, A.M.; Vu, M.-N.; Cui, Y.-J. Effects of the maximum soil aggregates size and cyclic wetting-drying on the stiffness of a lime-treated clayey soil. *Géotechnique* **2011**, *61*, 421–429. [CrossRef]
32. Wang, Y.; Cui, Y.J.; Benahmed, N.; Tang, A.M.; Duc, M. Changes of small strain shear modulus and suction for a lime-treated silt during curing. *Géotechnique* **2020**, *70*, 276–280. [CrossRef]
33. Muzahim, A.L.; Jean-Francois, A. Behaviour and mineralogy changes in lime-treated expansive soil at 50 °C. *Appl. Clay Sci.* **2010**, *50*, 199–203.
34. Bell, F.G. Lime stabilization of clay minerals and soils. *Eng. Geol.* **1996**, *42*, 223–237. [CrossRef]
35. Gautam, S.; Hoyos, L.R.; He, S.; Prabakar, S.; Yu, X.B. Chemical Treatment of a Highly Expansive Clay Using a Liquid Ionic Soil Stabilizer. *Geotech. Geol. Eng.* **2020**, *38*, 4981–4993. [CrossRef]
36. Xiang, W.; Cui, D.S.; Liu, Q.B.; Lu, X.S.; Cao, L.J. Theory and practice of ionic soil stabilizer reinforcing special clay. *J. Asian Earth Sci.* **2010**, *21*, 882–887. [CrossRef]
37. Luo, X.H.; Xu, W.Y.; Qiu, X.; Yang, Q.; Xiao, S.L. Exploring the microstructure characteristics and mechanical behavior of the ionic soil stabilizer-treated clay. *Arab. J. Geosci.* **2020**, *13*, 729. [CrossRef]
38. He, S.; Yu, X.B.; Banerjee, A.; Puppala, A.J. Expansive Soil Treatment with Liquid Ionic Soil Stabilizer. *Transp. Res. Rec.* **2018**, *2672*, 185–194. [CrossRef]
39. Wu, X.T.; Sun, J.S.; Qi, Y.; Chen, B. Pore and compression characteristics of clay solidified by ionic soil stabilizer Influence of soil initial state on clay solidification effect. *Bull. Eng. Geol. Environ.* **2021**, *80*, 5003–5019. [CrossRef]
40. Gong, X.; Niu, J.G.; Liang, S.H.; Feng, D.L.; Luo, Q.Z. Solidification of Nansha soft clay using cement-based composite curing agents. *Adv. Cem. Res.* **2020**, *32*, 66–77. [CrossRef]
41. Chen, N.; Wei, Y.Q.; Lu, J.F.; Li, G. Environmentally friendly solidifying agent for soft silty soil and its application in green foundation treatment. *Fresenius Environ. Bull.* **2020**, *29*, 6898–6905.
42. Liu, C.B.; Ji, H.G.; Liu, J.H. Anti-seawater corrosion performance of coastal saline soil solidified by slag composite cementitious material. *Emerg. Mater. Res.* **2014**, *3*, 292–298. [CrossRef]
43. Ma, C.; Qin, Z.H.; Zhuang, Y.C.; Chen, L.Z.; Chen, B. Influence of sodium silicate and promoters on unconfined compressive strength of Portland cement-stabilized clay. *Soils Found.* **2015**, *55*, 1222–1232. [CrossRef]
44. Koliji, A.; Laloui, L.; Vulliet, L. Constitutive modeling of unsaturated aggregated soils. *Int. J. Numer. Anal. Methods Geomech.* **2010**, *34*, 1846–1876. [CrossRef]
45. Liu, W.Z.; Shi, M.L.; Miao, L.C. Constitutive modeling of the destructuration and anisotropy of natural soft clay. *Comput. Geotech.* **2013**, *51*, 24–41. [CrossRef]
46. Pham, H.Q.; Fredlund, D.G. Volume-mass unsaturated soil constitutive model for drying-wetting under isotropic loading-unloading conditions. *Can. Geotech. J.* **2011**, *48*, 280–313. [CrossRef]
47. Anandarajah, A. Multi-mechanism anisotropic model for granular materials. *Int. J. Plast.* **2008**, *24*, 804–846. [CrossRef]
48. Viyalov, S.S. *The Strength and Creep of Frozen Soils*; U.S. Army CRREL: Hanover, NH, USA, 1962; Volume 74.
49. Lai, Y.; Xu, X.; Yu, W.; Qi, J. An experimental investigation of the mechanical behavior and a hyperplastic constitutive model of frozen loess. *Int. J. Eng. Sci.* **2014**, *84*, 29–53. [CrossRef]
50. Xu, G.F.; Wu, W.; Qi, J.L. Modeling the viscous behavior of frozen soil with hypoplasticity. *Int. J. Numer. Anal. Methods Geomech.* **2016**, *40*, 2061–2075. [CrossRef]
51. De Maeijer, P.K.; Craeye, B.; Snellings, R.; Kazemi-Kamyab, H.; Loots, M.; Janssens, K.; Nuyts, G. Effect of ultra-fine fly ash on concrete performance and durability. *Constr. Build. Mater.* **2020**, *263*, 120493. [CrossRef]
52. Ouhadi, V.R.; Yong, R.N. The role of clay fractions of marly soils on their post stabilization failure. *Eng. Geol.* **2003**, *70*, 365–375. [CrossRef]
53. Chen, K.Z.; Huang, S.; Liu, Y.J. Improving Carbonate Saline Soil in a Seasonally Frozen Region Using Lime and Fly Ash. *Geofluids* **2022**, *2022*, 7472284. [CrossRef]
54. Liao, M.; Lai, Y.M.; Wang, C. A strength criterion for frozen sodium sulfate saline soil. *Can. Geotech. J.* **2016**, *53*, 1176–1185. [CrossRef]
55. Sun, D.Y. *Mechanical Properties and Mechanism of Unsaturated Saline Soils and Lime Consolidated Soils in Zhenlai Area under Freeze-thaw Cycles*; Jilin University: Changchun, China, 2017.
56. Zheng, T.Y.; Zheng, Y. A review of earthquake disaster losses in mainland China in 2013. *J. Nat. Hazards* **2015**, *24*, 239–246.
57. Hu, T.F.; Liu, J.K.; Wang, Q.Z.; Fang, J.H. Experimental study on the undrained shear properties of powdered clay under freeze-thaw cycles. *J. Cent. South Univ.* **2018**, *49*, 1481–1490.

58. Niu, J.Y.; Jin, P.W.; Li, D.W. Study of the uniaxial compressive strength of frozen saline sandy soil. *J. Glaciol. Geocryol.* **2015**, *2*, 428–433.
59. Liu, Y.W.; Wang, Q.; Liu, S.W. Experimental investigation of the geotechnical properties and microstructure of lime-stabilized saline soils under freeze-thaw cycling. *Cold Reg. Sci. Technol.* **2019**, *161*, 32–42. [CrossRef]
60. Jean, L. How to use damage mechanics. *Nucl. Eng. Des.* **1984**, *80*, 233–245.
61. Zhang, Q.S.; Yang, Q.S.; Ren, J.X. A new approach to rock damage variables and intrinsic constitutive equations. *J. Rock Mech. Geotech.* **2003**, *1*, 30–34.